How to cite: *Angew. Chem. Int. Ed.* **2023,** *62,* e202301607
International Edition: doi.org/10.1002/anie.202301607
German Edition: doi.org/10.1002/ange.202301607

Protein Engineering

Harnessing the Structure and Dynamics of the Squalene-Hopene Cyclase for (−)-Ambroxide Production**

Andreas Schneider[+], Christian Curado[+], Thomas B. Lystbaek, Sílvia Osuna, and Bernhard Hauer**

Abstract: Terpene cyclases offer enormous synthetic potential, given their unique ability to forge complex hydrocarbon scaffolds from achiral precursors within a single cationic rearrangement cascade. Harnessing their synthetic power, however, has proved to be challenging owing to their generally low catalytic performance. In this study, we unveiled the catalytic potential of the squalene-hopene cyclase (SHC) by harnessing its structure and dynamics. First, we synergistically tailored the active site and entrance tunnel of the enzyme to generate a 397-fold improved (−)-ambroxide synthase. Our computational investigations explain how the introduced mutations work in concert to improve substrate acquisition, flow, and chaperoning. Kinetics, however, showed terpene-induced inactivation of the membrane-bound SHC to be the major turnover limitation in vivo. Merging this insight with the improved and stereoselective catalysis of the enzyme, we applied a feeding strategy to exceed 10^5 total turnovers. We believe that our results may bridge the gap for broader application of SHCs in synthetic chemistry.

[*] Dr. A. Schneider,[+] T. B. Lystbaek, Prof. B. Hauer
Department of Technical Biochemistry,
Institute of Biochemistry and Technical Biochemistry,
University of Stuttgart
Stuttgart-Vaihingen (Germany)
E-mail: Bernhard.Hauer@itb.uni-stuttgart.de

Dr. C. Curado,[+] Prof. S. Osuna
CompBioLab Group,
Institut de Química Computacional i Catàlisi and Departament de Química,
Universitat de Girona
Girona (Spain)
E-mail: silvia.osuna@udg.edu

Prof. S. Osuna
ICREA
Barcelona (Spain)

[+] These authors contributed equally to this work.

[**] A previous version of this manuscript has been deposited on a preprint server (https://doi.org/10.26434/chemrxiv-2022-xwcqj).

Introduction

The ability to generate (poly−)cyclic terpene scaffolds in a precise spatial arrangement renders terpene cyclases particularly useful catalysts for synthetic chemistry.[1,2] Their unique catalysis is facilitated by a strongly confined cation cage, which nature evolved to perfectly chaperone their substrates and guide the transient cations during cyclization.[3] As a consequence, cyclase enzymologists primarily focused on studying the active site, to shed light on the mechanistic details of a cationic cyclization cascade[4–6] or to expand the substrate and reaction scope, for example, of the squalene-hopene cyclase (SHC).[7,8] Despite substantial progress in this field, a persistent limitation in applying cyclases is their generally low catalytic performance (total turnover numbers, TTNs $< 10^3$)[1,2,9,10] as compared to other enzyme families, such as monooxygenases, transaminases or lipases with TTNs in the range of 10^5–10^7.[11] As a result, investigating cyclases in regions distal from the active site and assessing them in a more holistic way could serve as a potent solution.

This strategy becomes evident considering the recent success in identifying and overcoming catalytic bottlenecks by computationally analyzing dynamic elements, such as tunnels,[12,13] conformational landscapes,[14,15] or dynamic networks in enzymes.[16–18] For the supramolecular framework, that is the structure and topology, of SHCs, the situation gets even more complex (Figure 1A): These enzymes hold a unique role in enzymology as monotopic membrane-bound enzymes, accounting for only 0.06 % of all crystallized protein structures.[19] Nature evolved these interfacial proteins to provide them the catalytic skills of their soluble congeners, but with the additional ability to source highly hydrophobic C_{30} squalene from their host's biomembrane. In fact, SHCs regulate the membrane integrity of their biological host by depositing generated pentacyclic hopenes (Figure 1A, orange scaffold) in the membrane interior.[20–22] Conversely, seminal theoretical as well as experimental studies indicate that the activity of membrane-bound enzymes relies on the current state of the membrane integrity, which is drastically influenced by terpenes.[23–28]

In this study, we addressed the question of how to overcome the catalytic limitations in SHC catalysis by combining experimental enzyme engineering with computational aid and analysis. In addition to active-site mutagenesis usually applied in cyclase enzymology, we engineered the entrance tunnel and demonstrate the synergy of such an approach. Moreover, acknowledging the membrane-bound

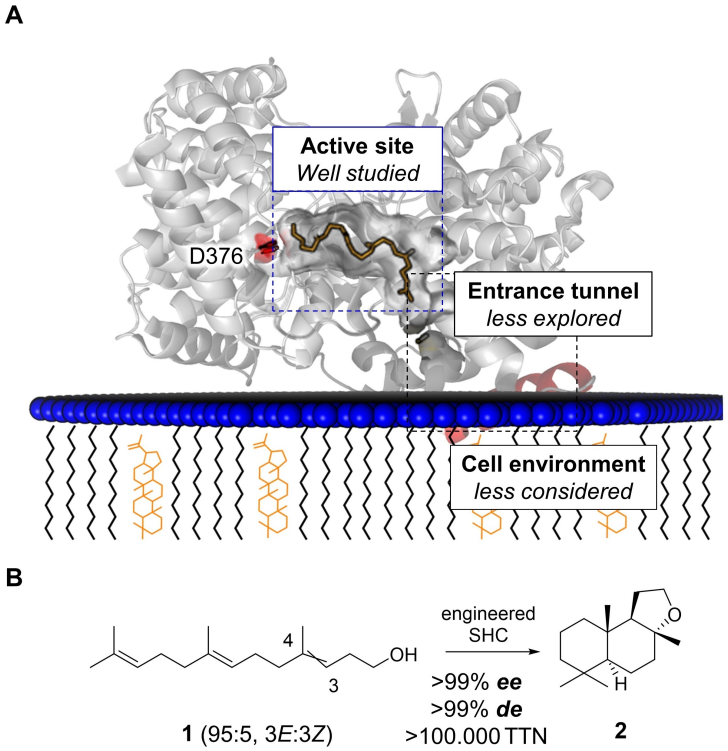

Figure 1. Overcoming the turnover limitations in SHC catalysis. A) SHCs (gray cartoon, PDB: 1UMP) are bound to their host's biomembrane (blue headgroups and black tails) by a reentrant α-helix (red cartoon), which classifies them as monotopic membrane enzymes.[19] Naturally, they regulate the biomembrane integrity by producing hopenes (orange scaffolds) from squalene (orange sticks) in their active sites (blue dashed lines) to counteract exterior stresses, such as temperature fluctuations or molecular toxification by lipophilic molecules.[22] The substrate is sourced from the membrane through a nonpolar tunnel (gray surface, black dashed lines).[29,30] Protonating D376 shown as red sticks. B) Engineering and reaction design efforts in this study were focused on the model cyclization of 95 : 5 3E : 3Z-homofarnesol (**1**) to fragrance compound (−)-ambroxide **2**, which we enabled with unprecedented stereocontrol (cf. with refs. [9 and 31]) and turnover numbers in the 10^5 range.

nature of SHCs, we aimed to investigate the enzyme-host relationship by kinetically contrasting the SHC in an artificial membrane-bound (in vitro) and biomembrane-bound (in vivo) state, which was scarcely considered in SHC biocatalysis.

As a model reaction for this endeavor, we chose the archetypical promiscuous cyclization of (3*E*)-homofarnesol (**1**) to (−)-ambroxide (**2**; Figure 1B). This reaction offers several advantages and opportunities: a) Catalysis has been shown to work both in vitro and in vivo;[9,32–34] b) as only product **2** crystallizes from the reaction broth, absolute selectivity towards **2** can be leveraged to overcome potential terpene-induced downregulation; c) product **2** is one of the highest valued fragrances in the industry, and the highly stereoselective cyclization of **1** towards **2**, catalyzed by the SHC from *Alicyclobacillus acidocaldarius* (*Aac*SHC), provides a potent substitute for the scarce natural availability of **2**,[35] especially since its chemical synthesis is complex, requires harsh conditions and is inferior in terms of selectivity (75 % *ee* and 67 % *de*).[31] These factors render the promiscuous cyclization of **1** ideally suited for a comprehensive investigation on SHC catalysis to cross its current catalytic boundaries.

Results and Discussion

To achieve this overarching goal, the first stage was to attain absolute control over the cationic cyclization of **1** by means of stereo- and product selectivity (Scheme 1), as the

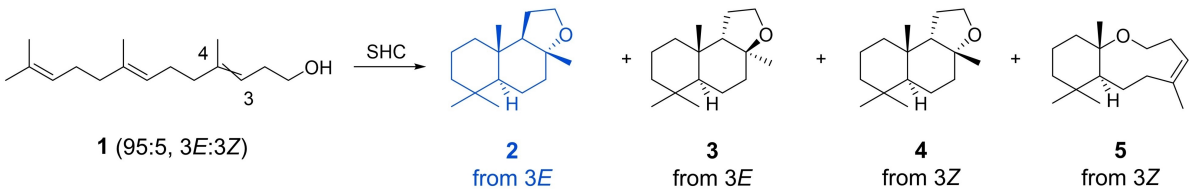

Scheme 1. AacSHC-catalyzed cationic cyclization of 95 : 5 3E : 3Z-homofarnesol (**1**) and the resulting products **2**–**5** from both epimers.[9]

biocatalysis should benefit from in situ product crystallization (ISPC) of **2** alone.[36]

In an earlier study, we reported how to control cationic cyclization cascades by introducing/breaking hydrogen bonds between a functional group in the substrate and adjacent active-site polar amino acids of terpene cyclases.[1] Following this structure-guided approach, we docked **1** into the active site of the *Aac*SHC wild type (WT) crystal structure, identified four amino acid residues (W169, I261, G600, F601) within 5 Å of the alcohol group of **2** (Figure 2A), randomized those by the 22c-trick[37] and screened the resulting variants directly in their expressing *E. coli* host (in vivo), using 95:5, 3*E*:3*Z*-homofarnesol (**1**). To emphasize our engineering efforts, the actual *Aac*SHC benchmark variant[9] B is also depicted in Figure 2B. Screening 360 variants revealed positions 600 and 169 as most beneficial for the cyclization (Figure S1), of which variant W169G, that is, P1, showed 108-fold increased turnover frequency (TOF) of 24 h^{-1} as compared to the WT and the desired excellent selectivity of 99 % (Figure 2B). Next, we targeted six more residues, L607, G600, L36, A306, S307, and I261, that are located within the 5 Å radius and performed one additional round of site-saturation mutagenesis.

Screening of 540 generated variants resulted in double-variant W169G/G600M, that is, P2, which showed 2.7-fold increase in turnover frequency (TOF) of 64.6 h^{-1} while retaining >99 mol % selectivity for **2**. Further mutations in the active site disrupted the high selectivity of the enzyme, which encouraged us to discover alternative mutation hot spots, located distal from the active site. Consequently, we performed a CAVER[38] analysis of the *Aac*SHC crystal structure, which revealed several potential tunnels (Figure S4), of which we focused on the suggested enzyme entrance tunnel (Figure 2C, blue surface).[29] Notably, two (M132R/I432T) out of three positions (M132R/A224V/I432T) of B were located in the designated bottleneck area, with the third position described by the authors themselves as not beneficial.[9] These results gave reason to perform

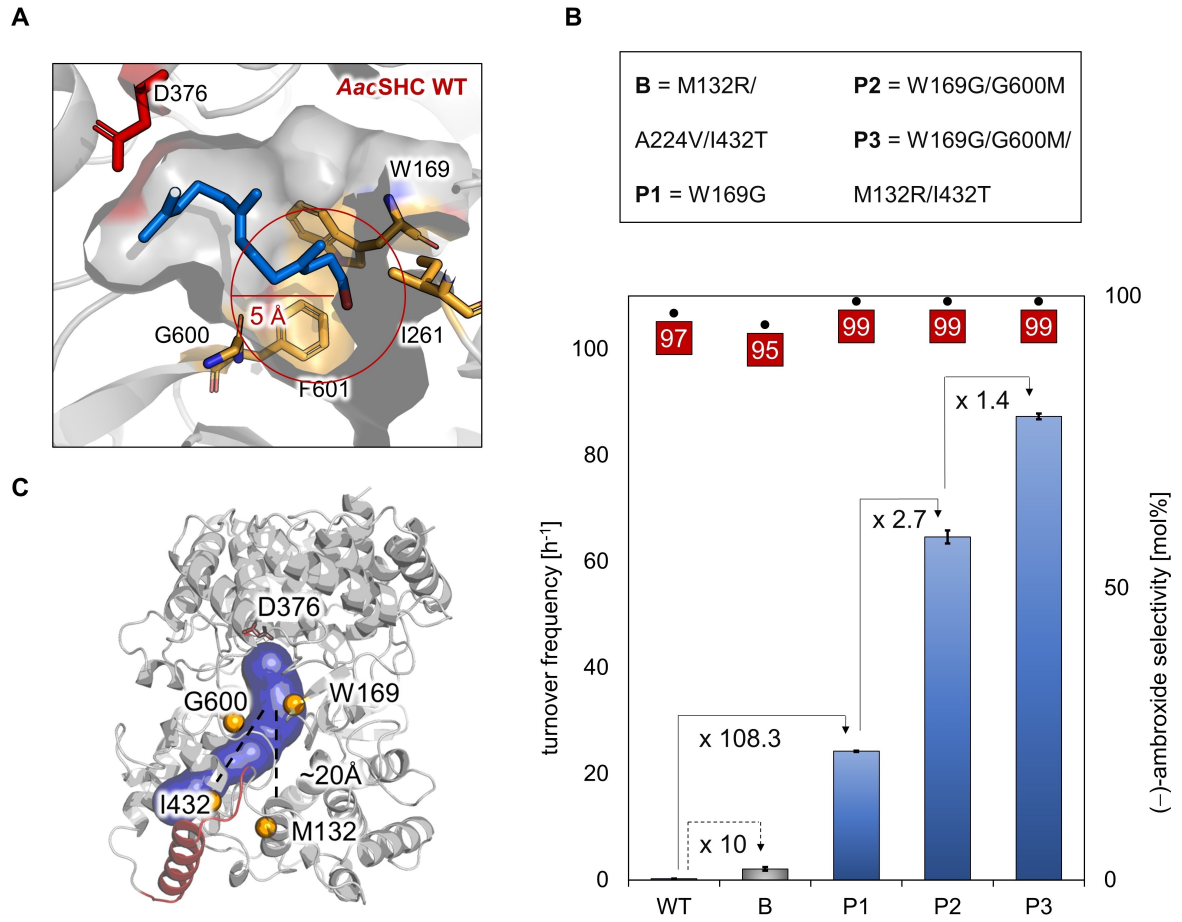

Figure 2. Engineering AacSHC towards highly efficient (−)-ambroxide (**2**) production under process conditions.[9] A) Docking of (E,E)-homofarnesol (**1**; blue sticks) into the active site of the AacSHC wild type (WT; PDB: 1UMP). Amino acid positions targeted for mutagenesis are shown as yellow sticks and protonating D376 as red sticks. B) Overall engineering of AacSHC. Variants are plotted against their turnover frequency (left y-axis) and their selectivity for (−)-ambroxide (**2**) in mol % (right y-axis). Reaction conditions: 1 mL ddH_2O + 0.2 % SDS, 10 mg_{CDW} E. coli whole cells harboring the corresponding AacSHC variant (40–50 μM), 100 mM (ca. 50 $g\,L^{-1}$) (E,E)-**1**, 19 h, 30 °C, 750 rpm. Error bars represent the standard deviation of technical triplicates. For screening conditions, see Figures S2 and S3. C) Crystal structure of AacSHC WT with the putative entrance tunnel in blue and membrane binding α-helix in red. Mutated amino acid locations are shown as yellow spheres and protonating D376 as red sticks. Distance of entrance tunnel mutations to the alcohol group of **1** shown as dashed lines.

site-saturation mutagenesis within this bottleneck area, which unexpectedly resulted in only slight to no increases in TOF (Figure S5). However, the addition of both published distal mutations (M132R/I432T) resulted in the final variant P3 with a 1.3-fold increase in TOF to 87.3 h^{-1} and no loss of selectivity.

Summing up, our enzyme engineering efforts improved the overall rate of the native enzyme by a factor of 397, while ensuring excellent stereocontrol over the cyclization of **1**. The catalysis under in vivo process conditions clearly benefits from the exclusive cyclization selectivity towards **2** (see Figure S3), which may be the result of the continuous ISPC, which avoids membrane-disturbing liquid side products. Remarkably, the 95:5, 3*E*:3*Z* substrate **1** mixture was converted with >99 mol % selectivity into the same stereoisomer (−)-ambroxide (**2**), which suggests an unprecedented stereoconvergent cationic cyclization of a terpene isomeric mixture. The overall catalytic performance was improved by a dual-site targeted mutagenesis approach, which was presented in a similar way by the Reetz group during their engineering of a monoamine oxidase.[39] Such dual-site targeted approaches extend the strategy of active-site mutagenesis usually conducted in terpene cyclase studies[30,40–42] and are also a useful extension in the portfolio of rational enzyme engineering strategies.

To rationalize the effects of the introduced active-site and distal mutations on the enzyme structure and the accompanied improvement in their catalytic efficiency, a deep computational exploration was performed by means of molecular dynamics (MD) simulations (see the Supporting Information for details). We reconstructed the conformational landscapes of WT and P variants by analyzing the gathered MD data using principal component analysis (PCA; Figure 3). The analysis was based on distances between active-site residues (6 Å from its center of mass, see the Supporting Information for details) to reveal the key active-site conformational differences that explain the improved catalytic power of P variants.[15]

For WT, three main conformations of the active-site residues were observed (Figure 3A): *conformation 1* displays

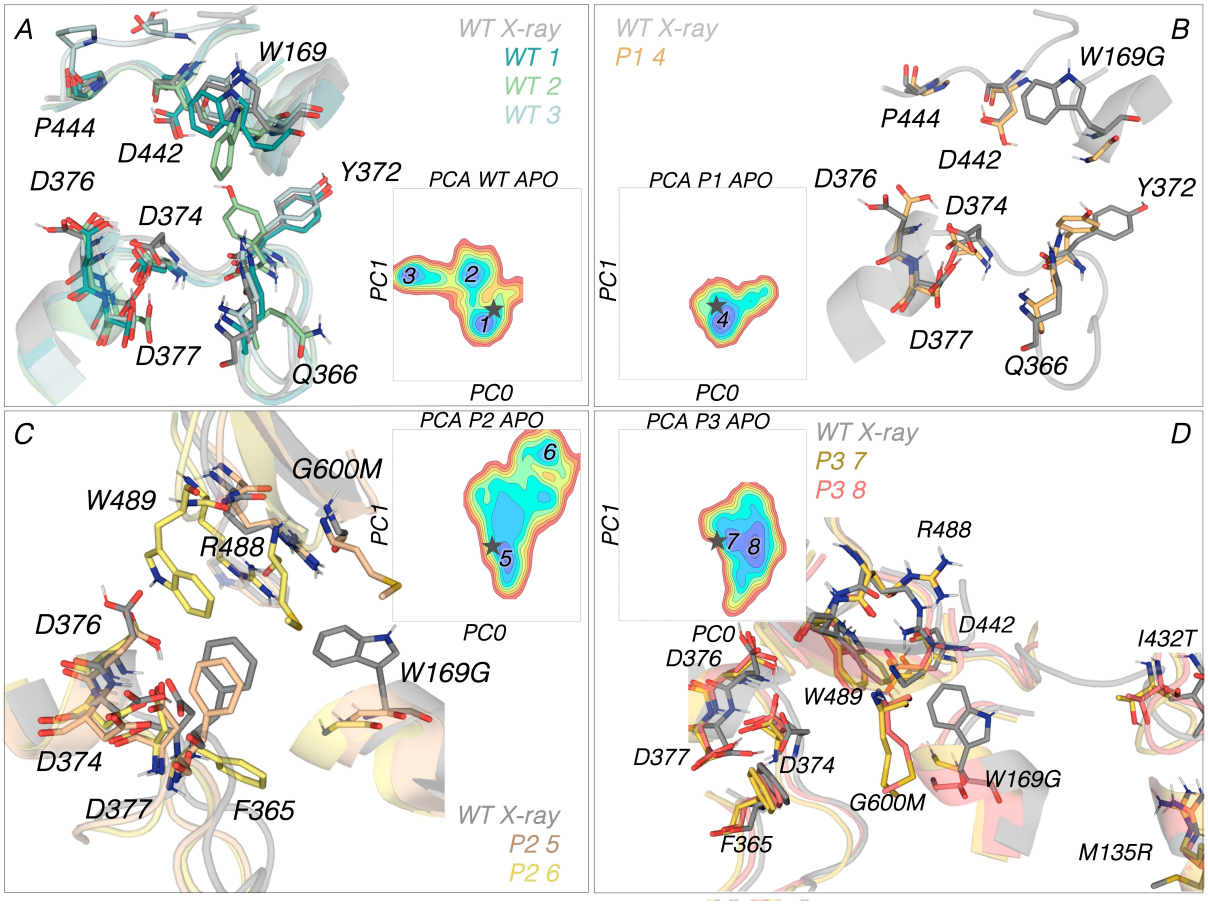

Figure 3. Analysis of the conformational changes induced by the mutations in the different AacSHC variants. Conformational landscapes as described by principal component analysis (PCA) of A) AacSHC WT, B) P1, C) P2, and D) P3 variants showing the most populated conformations in blue and the least populated conformations in red. Overlay of each conformation from the conformational landscape of A) AacSHC WT, B) P1, C) P2, and D) P3 variants with the crystal structure included as reference (shown in gray, PDB: 1UMP). The most important active-site residues are labeled, and different colors are used to represent the different representative conformations extracted from each minimum in the conformational landscape. The gray star in each conformational landscape indicates where the conformation of the crystal structure is located in the generated PC space.

an orientation of the active-site residues that is similar to that in the X-ray crystal structure; *conf. 2* involves a reshaping of the active site, resulting from a flip of residues W169, Q366, D442, and Y372; and *conf. 3* is similar to *1* but presents a different disposition of the loop containing P444. Additionally, a side-chain rotation of Y372 that may hamper the accessibility to the catalytic aspartic triad is observed in *conf. 3*.

In the case of P1, a single X-ray-structure-like active-site conformation was explored in the accumulated MD simulation time (Figure 3B, *conf. 4*). The main conformational difference with respect to WT is the rotation of side chain Y372, which interacts with the backbone of residue G169. As illustrated in Figure 3C, P2 adopts two main conformations: the X-ray-structure-like *conf. 5*, and *conf. 6*, in which a drastic reorganization of the active site is observed. While the W169G mutation alone simply expanded the active-site pocket, its combination with mutation G600M results in a dramatic effect on its size and shape. In particular, both mutations act synergistically and introduce a new interaction between R488 and the backbone of mutation G600M. Consequently, the position of W489 is altered allowing better interaction with the catalytic D376 residue. Finally, the introduced steric bulk at position 600 induces a side-chain rotation of F365. Notwithstanding, and considering the orientation of the latter, this conformation could be impeding the proper access of **2** through the substrate entrance tunnel. As observed for all variants, P3 adopts *conf. 7*, which resembles the conformation of the active site in the X-ray crystal structure, and *conf. 8*, which is similar to *conf. 7* (Figure 3D). Therefore, the increasing effect of the catalytic efficiency by the distal mutations M132R and I432T may be attributed to the substrate flow and tunnel dynamics that could facilitate the binding process.

To unravel this hypothesis, tunnel analyses were performed on each displayed conformation of WT, P1, P2, and P3 variants, thus leading to the complete reconstruction of tunnel dynamics along all conformational landscapes. As shown in Table 1, the average bottleneck radius (avgBR) is similar in all conformations and systems, and lies between 0.93 and 1.15 Å. However, drastic differences in the populations of the substrate entrance tunnel were obtained, thus indicating that this parameter has been tuned by the mutations introduced by the laboratory-engineering strategy.

Table 1: Tunnel analysis for each conformation of every variant (see Figure 3), the average bottleneck radius (avgBR), maximum bottleneck radius (maxBR) expressed in angstroms, and the percentage population of the computed substrate entrance tunnel are displayed (i.e. percentage of structures in which the tunnel exists).

Variant	Conformation	avgBR [Å]	maxBR [Å]	Population [%]
WT	1	0.95 ± 0.06	1.19	5
WT	2	0.98 ± 0.07	1.17	3
WT	3	0.97 ± 0.07	1.24	29
P1	4	1.03 ± 0.12	1.45	28
P2	5	1.07 ± 0.13	1.58	29
P2	6	0.93 ± 0.03	1.01	5
P3	7	1.15 ± 0.26	1.83	38
P3	8	1.05 ± 0.15	1.74	58

By analyzing the substrate entrance tunnel for each conformation of the WT enzyme we observed low populations for *conf. 1* and *2*, whereas *conf. 3* displayed a higher population of the tunnel (ca. 29 %). However, our estimated conformational landscape suggests this conformation can only be accessed by a relatively high energy barrier, which may explain the limited catalytic efficiency (see Figure 3). The single mutation introduced in P1 enhances the population of the substrate entrance tunnel with respect to WT, as a population of 28 % is found for the main *conf. 4* and presents a slightly higher bottleneck radius. Variant P2 can adopt two main conformations: *conf. 5* presenting a tunnel population of 29 % and a bottleneck radius of 1.07 Å, and *conf. 6* presenting only 5 % of the analyzed snapshots with the main substrate entrance tunnel formed. Our estimated conformational landscapes suggest a rather low stability of *conf. 6* with respect to *5*, and a rather high energy barrier for the conformational transition.

Finally, in the case of P3, we observed high populations of the substrate entrance tunnel for both conformations: 38 % population in *conf. 7* and 58 % in *conf. 8*, displaying an average bottleneck radius of approximately 1.1 Å in both conformations. This increase in the tunnel population for the two main conformations adopted by P3 might be one of the main reasons behind the improved activity of P3 with respect to the other engineered P variants.

In our final investigation we were interested in the ability of the most engineered enzymes to pre-fold **1** in their active sites as well as the resulting conformational changes upon substrate binding. For this purpose, we performed molecular docking of the substrate **1** into the most populated conformations observed in the apo-enzymes, followed by MD refinement and conformational landscape reconstruction by analyzing the catalytic distance and angle (Figure S6B). Productive binding was defined by protonating hydrogen (D376) to nucleophile carbon distance D_{prot} below 4.5 Å and an angle Θ_{prot} between 40 and 60° (Figure 4A).[43]

When analyzing P2, we again observed the synergy of the two introduced mutations W169G and G600M. The extra room generated by mutation W169G leaves enough space for the G600M side chain, which is pointing to the center of the active site. This side-chain reorganization is responsible for the better chaperoning of **1**, shortening D_{prot} and improving Θ_{prot} (Figure 4B). Intriguingly, even more suitable pre-folding of **1** can be observed in P3, which includes the tunnel mutations M132R and I432T approximately 20 Å away. Despite their distance, these mutations drastically affect the size and shape of the catalytic pocket by means of a network of interactions that lead to side-chain reorganizations. More specifically, M132R (in combination with all other mutations) seems to be responsible for triggering such reorganization (Figure 3B). The new arginine side chain introduced (M132R) can interact with the backbone of residue F434. This new interaction between R132 and F434 leads to a flip in the loop containing F437, which generates extra space that is occupied by the side chain of

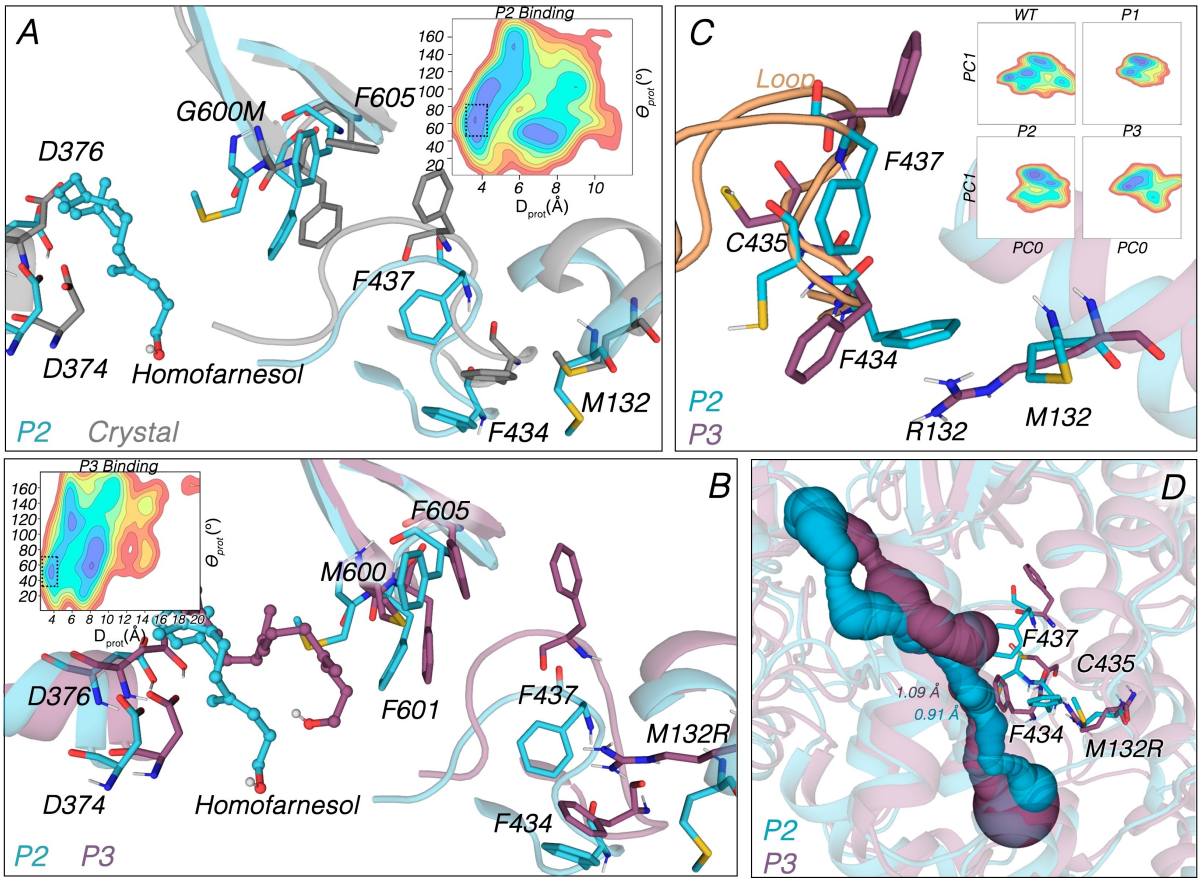

Figure 4. Comparison of the conformational changes of active site residues upon substrate binding, loop containing F434, and impact on substrate tunnels on P2 and P3 variants. Substrate binding conformational landscape for A) P2 (light-blue) and B) P3 (purple) variants based on the computed catalytic D_{prot} (in Å) and Θ_{prot} (in degrees). In the conformational landscape, most populated conformations are shown in blue, whereas least populated ones are in red. An overlay of representative MD snapshots from the selected regions (marked with dashed black squares) of the binding conformational landscape representing the binding of **2** in the active site for P2 (green) and P3 variants. C) Conformational landscape of the loop containing F434. Overlay of P2 (blue) and P3 (purple) conformations (for a better representation, WT and P1 were not included, see Figure S7). Most populated conformations are shown in the conformational landscape in blue, whereas less populated conformations are shown in red. D) Overlay of the substrate tunnel in the different conformations of the loop in P2 (blue) and P3 (purple). Bottleneck radii are displayed in angstroms.

F605. This results in a higher flexibility of M600 that enables **1** to adopt more pre-folded conformations, with improved D_{prot} and Θ_{prot}.

The new network of interactions in P3 may be stabilizing wider substrate tunnels in the P3 variant, which could be translated into higher displayed activities over P2. To unravel this hypothesis, PCA analyses were conducted on the loop containing residue F437, aiming to determine which conformations are mainly adopted by each variant (Figure 4C and Figure S7). As we observed in **1**-bound MD simulations, mutation M132R in the P3 variant stabilizes the X-ray-structure-like orientation of the loop. This new mutation produces a flip in residue F434, which alters the backbone dihedral angle of residue C435. Furthermore, the latter determines the orientation of the side chain of residue F437. This network of coupled conformational changes produces a wider substrate tunnel that is reflected in the previously analyzed tunnels (Figure 4D). Interestingly, the conformations of the F434-containing loop that resemble the X-ray crystal structure resulted in a pre-folded binding of **1** in the case of P3, whereas in the case of P2 there is a flip of this F434-loop that induces the stretching and unbinding of **1** (see Figure 3B). Indeed, F437 and C435 residues were identified as key gating residues in a previous study, which is also supported by our MD simulations.[30]

Taking our computational results together, we demonstrated that the active-site mutations are mainly responsible for the reorganization of the active site and improved chaperoning of **1**, especially in P2 and P3 variants, whereas the tunnel mutations are mainly responsible for an improved substrate flux stabilizing the X-ray-structure-like conformations of the loop containing F434. These findings suggest that we achieved the 397-fold improved catalyst by tailoring the supramolecular and dynamic SHC scaffold for a "wider tunnel" catalyst with improved substrate flux and chaperoning.

The next step towards the overarching aim to exceed the turnover limits of SHC was to investigate the performance

of the enzyme with high substrate to cell or catalyst ratios. After some initial experiments that demonstrated cell-concentration-dependent activity and long-term operational enzyme stability—a reaction time of about 42 days—of the enzyme in vivo (Figure S8), the four *Aac*SHC variants WT, B, P2 and P3 were kinetically analyzed in vivo and in vitro (Figure 5A, B). These variants were chosen as they encompass the four stages of engineering: native enzyme, engineered entrance tunnel, engineered active site, and engineered active site + entrance tunnel. Starting with the in vitro characterization, membrane-bound enzymes require detergents as an artificial membrane for isolation and solubilization, which may influence their catalytic activity.[32,44,45] The evaluation showed that the entrance tunnel mutations of the benchmark SHC B doubled the k_{cat} value, while only slightly affecting K_M and therefore substrate affinity (Table 2, B, in vitro). In P2, the alterations highly increased the substrate affinity and thus lowered the

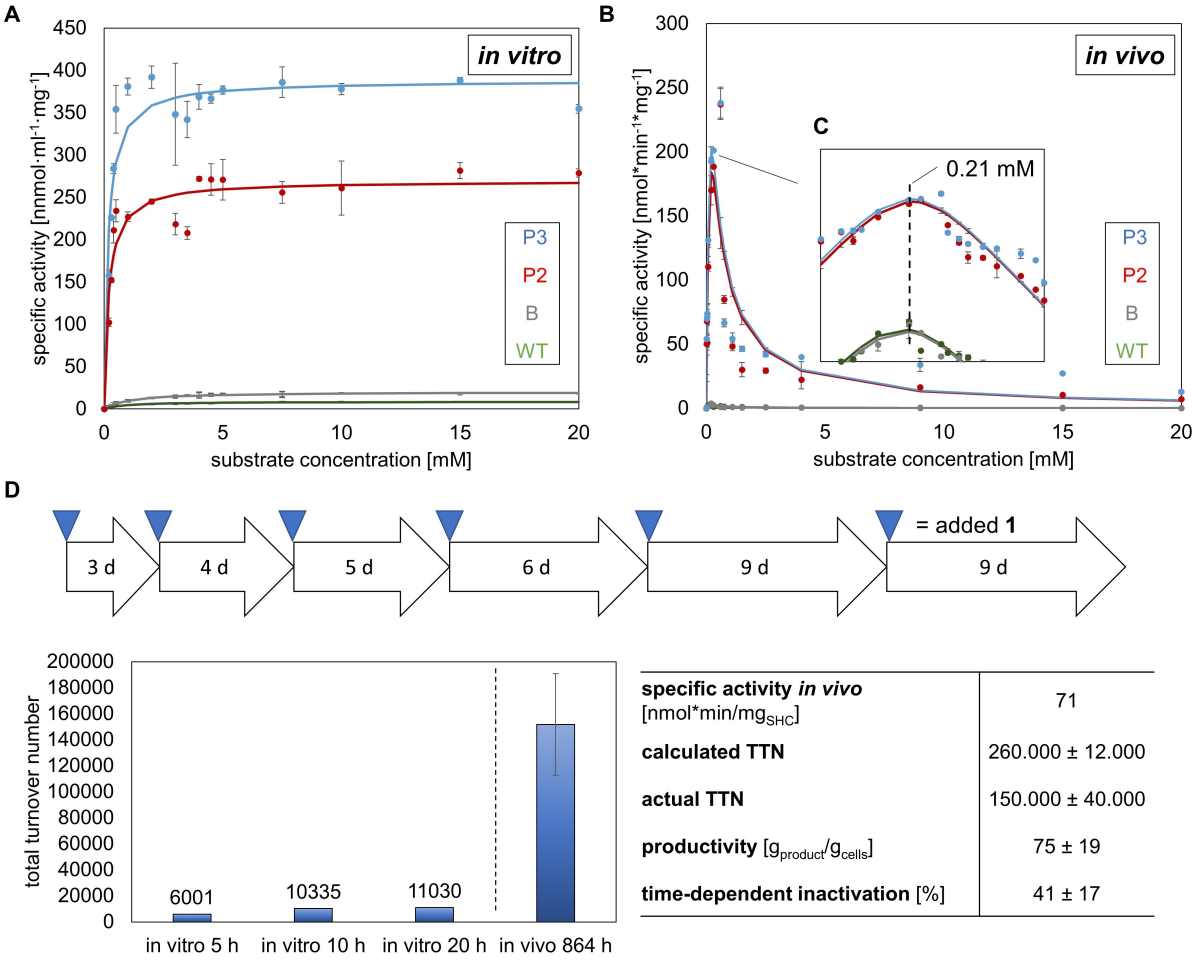

specific activity *in vivo* [nmol*min/mg$_{SHC}$]	71
calculated TTN	260.000 ± 12.000
actual TTN	150.000 ± 40.000
productivity [g$_{product}$/g$_{cells}$]	75 ± 19
time-dependent inactivation [%]	41 ± 17

Figure 5. Exceeding the turnover limits of the SHC. A) Michaelis–Menten plots for the cyclization of **1** catalyzed by AacSHC WT, B, P2, and P3 in vitro. B) Substrate-excess inhibition plots for the cyclization of **1** catalyzed by AacSHC WT, B, P2, and P3 in vivo. C) Double-logarithmic plot of substrate concentration versus specific activity. Error bars represent the standard deviation between technical triplicates. D) Feeding strategy for the maximum total turnover number (TTN) of **1** with an engineered P3 driven by continuous in situ product crystallization. Arrows only apply for long term in vivo approach. Calculated TTN was determined assuming the specific activity of 71 nmol min mg$_{SHC}^{-1}$, which was taken from Figure S9. Please see the Supporting Information for detailed reaction conditions and monitoring.

Table 2: Parameters of initial rate kinetics for *Aac*SHC WT and variants B, P2 and P3 in vitro and in vivo. The in vitro kinetics were fitted by Michaelis–Menten plots. The In vivo kinetics were fitted by substrate-excess inhibition plots. Errors denote the errors of the fitting.

	in vitro K_M [mM]	k_{cat} [min^{-1}]	k_{cat}/K_M [mM^{-1} min^{-1}]	in vivo $K_{M,app}$ [mM]	$k_{cat,app}$ [min^{-1}]	$k_{cat,app}/K_{M,app}$ [mM^{-1} min^{-1}]
WT	0.94 ± 0.08	1.4 ± 0.1	1.49 ± 0.02	0.16 ± 0.01	0.52 ± 0.07	3.2 ± 0.2
B	1.10 ± 0.12	2.9 ± 0.1	2.7 ± 0.2	0.17 ± 0.02	0.60 ± 0.05	3.5 ± 0.1
P2	0.19 ± 0.02	36 ± 4	188 ± 2	0.22 ± 0.04	26 ± 2	122 ± 13
P3	0.16 ± 0.03	62 ± 2	396 ± 59	0.21 ± 0.02	29 ± 1	137 ± 6

K_M value 5-fold, which entailed a 12-fold increase in k_{cat} (Table 2, P2, in vitro). Finally, the additional entrance tunnel mutations in P3 resulted in almost doubled k_{cat}, while minorly decreasing K_M as compared to P2. In total, the structure-guided engineering of the WT in the active site and entrance tunnel led to a catalytic efficiency k_{cat}/K_M of 396 mM min^{-1} (Table 2, P3, in vitro), which is an improvement of more than 260-fold. Remarkably, these experimental findings closely align with our computational data, which ascribed an increased tunnel population, and therefore the maximal reaction velocity of the enyzme, as the main benefit of P3 over P2.

Notably, all initial rate kinetics in vitro could be fitted by Michaelis–Menten plots (Figure 5A). In contrast, the in vivo kinetics had to be fitted by substrate-excess-inhibition plots with the inhibition constant $K_i = K_{M,app}$ occurring at approximately 0.21 mM for all characterized variants (Figure 5B, C). Nevertheless, a 43-fold increase in catalytic efficiency of P3 ($k_{cat,app}/K_{M,app} \approx 137$ mM min^{-1}) as compared to the WT was determined (Table 2, P3, in vivo). Interestingly, the strong inhibition was lowered by reducing the orbital shaking from 800 to 600 to 300 rpm at the expense of a 9-fold lower catalytic efficiency $k_{cat,app}/K_{M,app}$ of approximately 15 (Figure S9).

With this knowledge about the excellent biocatalyst stability in vivo and the enyzme kinetics, we envisaged a feeding strategy exploiting the stereoconvergence of the enzyme and the continuous ISPC of **2**. To that end, an enzyme solution (0.015 mg ml^{-1} SHC, 0.2 % CHAPS, 20 mM citric acid, pH 6.0) and whole-cell suspension (0.1 g_{CDW}/L in 20 mM citric acid, pH 6.0) were prepared, supplemented with 200 µL (7 mM) pure **1** and shaken at 300 rpm, and substrate depletion and product formation were measured by GC as well as observed optically. This particular substrate concentration was selected as it depicts the concentration before cross-over of the inhibited and non-inhibited in vivo plots (see Figure S9). During the in vitro approaches almost no depletion occurred, and the reactions stopped after about 10 h and 3.5 % product formation, which equals a total turnover number of approximately 11000. Intriguingly, the SHC in the whole cells was active for about 36 days using the feeding strategy (Figure 5D). Thus, an average total turnover number (TTN) of approximately 150000 was attained. As compared to the calculated TTN of approximately 260000, the enzyme lost about 41 % of its activity, indicating time-dependent inactivation of the catalyst. Overall, about 0.75 g of the desired product (−)-ambroxide (**2**) was produced by employing only 10 mg of *E. coli* whole cells (Figure 5D).

To sum up, the kinetic data disclosed meaningful differences in the catalytic behavior of the enzyme in vivo and in vitro. In their biomembrane environment, all SHC variants are strongly inhibited after the peak-performance concentration of 0.21 mM, which suggests a distinct function of the cell on the SHC activity. Considering this inseparable enzyme-host relationship was also the key to success in other studies employing monooxygenases.[46,47] Owing to their inherent hydrophobicity, terpenes diffuse into the hydrophobic core of the cellular membrane, presumably causing local perturbations[48] or cell death by membrane desintegration.[49] In the former case the enzyme could react by downregulating its activity, which would be a simple tool for nature to control the activity of membrane-bound enzymes as already hypothesized in 1975.[50] Independent of this scenario, high terpene concentrations require a hydrophobic sink, which can be achieved, for example, by the invagination of the cellular membrane[51] or simply by increasing the cell concentration.[9] In the present study, a feeding strategy combined with the exclusive selectivity and the in situ product crystallization of only **2** kept the enzyme stable for several weeks, performing $>10^5$ turnovers, which supersedes all so far reported TTNs of SHCs[2,7,9] and unveils the true potential of these enzymes. Biocatalysts exhibiting such turnover numbers are well-positioned among the upper ranks of industrially applied enzymes.[11,52] However, an apparent drawback is the long time period of the presented process, which could be overcome, for example, by increasing the mass transfer across the biomembrane using membrane transporter enzymes[53] or spheroplast preparation.[54] Furthermore, the herein presented in vitro approach could certainly be fine-tuned by changing the detergent, the detergent concentration or the buffer; however, such fine-tuning was beyond the scope of this study.

Conclusion

Harnessing the synthetic power of cyclases is of major importance for chemistry as they display unprecedented atom and step economy.[1] In this study we have demonstrated how to tailor and leverage the topology of SHCs to perform catalysis beyond their currently known capabilities. Total turnover limits were exceeded by synergistically widening the enzyme tunnel, adjusting substrate chaperoning and considering the inseparable enzyme-host relationship. In alignment with other seminal studies,[14,16] this highlights the undiscovered catalytic potential, which can be triggered by exploiting the whole supramolecular structure of an enzyme. A remarkable observation during this study was a stereoconvergent cationic cyclization that will be elucidated in detail in future work. Going forward, the exact mechanism of terpene-induced downregulation will be analyzed by studying the membrane properties during catalysis, for example, by fluorescence imaging.[55] Assuming such indirect downregulation of monotopically membrane bound enzymes opens up alternative views on diseases related to similar enzymes, such as the visual impairment, Alzheimer's or Parkinson's disease.[56–60] Because, in the words of Engasser and Horvath, "*It is unlikely that nature would not use such a simple tool to control and trigger physiological processes*".[23]

Author Contributions

A. S., B. H. and S. O. planned the overall project. A. S. and T. L. conducted experimental work. C. C. conducted compu-

tational work. A. S., C. C., B. H. and S. O. drafted the manuscript. All authors agreed on the final manuscript.

Acknowledgements

We thank Lea Rapp and Peter Heinemann for fruitful discussions. A. S. and B. H. gratefully acknowledge the Deutsche Forschungsgemeinschaft (DFG HA 1251/6-1) for research funding. C. C. and S. O. thank the Generalitat de Catalunya for the emerging group CompBioLab (2017 SGR-1707), and Spanish MINECO for projects PID2021-129034NB-I00 and PDC2022-133950-I00. C. C. was supported by a research grant from ERC-StG (ERC-2015-StG-679001). S. O. is grateful for funding from the European Research Council (ERC) under the European Union's Horizon 2020 research and innovation program (ERC-2015-StG-679001), and the Human Frontier Science Program (HFSP) for project grant RGP0054/2020. Open Access funding enabled and organized by Projekt DEAL.

Conflict of Interest

The authors declare no conflict of interest.

Data Availability Statement

The data that support the findings of this study are available in the supplementary material of this article.

Keywords: Biocatalysis · Brønsted Acid Catalysis · Cyclization · Sustainable Chemistry · Terpenoids

[1] A. Schneider, P. Jegl, B. Hauer, *Angew. Chem. Int. Ed.* **2021**, *60*, 13251–13256.
[2] M. Eichenberger, S. Hüppi, D. Patsch, N. Aeberli, R. Berweger, S. Dossenbach, E. Eichhorn, F. Flachsmann, L. Hortencio, F. Voirol, S. Vollenweider, U. T. Bornscheuer, R. Buller, *Angew. Chem. Int. Ed.* **2021**, *60*, 26080–26086.
[3] D. W. Christianson, *Chem. Rev.* **2017**, *117*, 11570–11648.
[4] D. Morrone, M. Xu, D. B. Fulton, M. K. Determan, R. J. Peters, *J. Am. Chem. Soc.* **2008**, *130*, 5400–5401.
[5] T. Hoshino, I. Kaneko, Y. Terasawa, *Chem. Eur. J.* **2018**, *24*, 37–47.
[6] N. Morikubo, Y. Fukuda, K. Ohtake, N. Shinya, D. Kiga, K. Sakamoto, M. Asanuma, H. Hirota, S. Yokoyama, T. Hoshino, *J. Am. Chem. Soc.* **2006**, *128*, 13184–13194.
[7] S. C. Hammer, A. Marjanovic, J. M. Dominicus, B. M. Nestl, B. Hauer, *Nat. Chem. Biol.* **2015**, *11*, 121–126.
[8] A. Schneider, J. Ruppert, T. B. Lystbæk, S. Bastian, B. Hauer, *ACS Catal.* **2023**, *13*, 1946–1951.
[9] E. Eichhorn, E. Locher, S. Guillemer, D. Wahler, L. Fourage, B. Schilling, *Adv. Synth. Catal.* **2018**, *360*, 2339–2351.
[10] K. Potter, J. Criswell, J. Zi, A. Stubbs, R. J. Peters, *Angew. Chem. Int. Ed.* **2014**, *53*, 7198–7202.
[11] S. Wu, R. Snajdrova, J. C. Moore, K. Baldenius, U. T. Bornscheuer, *Angew. Chem. Int. Ed.* **2021**, *60*, 88–119.
[12] L. R. Rapp, S. M. Marques, E. Zukic, B. Rowlinson, M. Sharma, G. Grogan, J. Damborsky, B. Hauer, *ACS Catal.* **2021**, *11*, 3182–3189.
[13] A. Gora, J. Brezovsky, J. Damborsky, *Chem. Rev.* **2013**, *113*, 5871–5923.
[14] R. Otten, R. A. P. Pádua, H. A. Bunzel, V. Nguyen, W. Pitsawong, M. Patterson, S. Sui, S. L. Perry, A. E. Cohen, D. Hilvert, D. Kern, *Science* **2020**, *370*, 1442–1446.
[15] M. A. Maria-Solano, E. Serrano-Hervás, A. Romero-Rivera, J. Iglesias-Fernández, S. Osuna, *Chem. Commun.* **2018**, *54*, 6622–6634.
[16] H. A. Bunzel, J. L. R. Anderson, D. Hilvert, V. L. Arcus, M. W. van der Kamp, A. J. Mulholland, *Nat. Chem.* **2021**, *13*, 1017–1022.
[17] S. Osuna, *Wiley Interdiscip. Rev.: Comput. Mol. Sci.* **2021**, *11*, e1502.
[18] M. A. Maria-Solano, T. Kinateder, J. Iglesias-Fernández, R. Sterner, S. Osuna, *ACS Catal.* **2021**, *11*, 13733–13743.
[19] K. N. Allen, S. Entova, L. C. Ray, B. Imperiali, *Trends Biochem. Sci.* **2019**, *44*, 7–20.
[20] G. Darland, T. D. Brock, *J. Gen. Microbiol.* **1971**, *67*, 9–15.
[21] K. Poralla, E. Kannenberg, A. Blume, *FEBS Lett.* **1980**, *113*, 107–110.
[22] B. J. Belin, N. Busset, E. Giraud, A. Molinaro, A. Silipo, Di. K. Newman, *Nat. Rev. Microbiol.* **2018**, *16*, 304–315.
[23] J.-M. Engasser, C. Horvath, *Biochemistry* **1974**, *13*, 26.
[24] K. Balali-Mood, P. J. Bond, M. S. P. Sansom, *Biochemistry* **2009**, *48*, 2135–2145.
[25] H. S. Camargos, R. A. Moreira, S. A. Mendanha, K. S. Fernandes, M. L. Dorta, A. Alonso, *PLoS One* **2014**, *9*, e104429.
[26] F. Harb, L. Prunetti, M. T. Giudici-Orticoni, M. Guiral, B. Tinland, *Eur. Phys. J. E* **2015**, *38*, 110.
[27] A. H. Pande, S. Qin, S. A. Tatulian, *Biophys. J.* **2005**, *88*, 4084–4094.
[28] A. Laganowsky, E. Reading, T. M. Allison, M. B. Ulmschneider, M. T. Degiacomi, A. J. Baldwin, C. V. Robinson, *Nature* **2014**, *510*, 172–175.
[29] K. U. Wendt, K. Poralla, G. E. Schulz, *Science* **1997**, *277*, 1811–1815.
[30] T. Sato, M. Kouda, T. Hoshino, *Biosci. Biotechnol. Biochem.* **2004**, *68*, 728–738.
[31] K. Ishihara, H. Ishibashi, H. Yamamoto, *J. Am. Chem. Soc.* **2002**, *124*, 3647–3655.
[32] S. Neumann, H. Simon, *Biol. Chem. Hoppe-Seyler* **1986**, *367*, 723–730.
[33] M. Seitz, J. Klebensberger, S. Siebenhaller, M. Breuer, G. Siedenburg, D. Jendrossek, B. Hauer, *J. Mol. Catal. B* **2012**, *84*, 72–77.
[34] M. Breuer, A. Hörster, B. Hauer (BASF), U.S. Patent No. 8, 759, 043, **2014**.
[35] S. J. Rowland, P. A. Sutton, T. D. J. Knowles, *Nat. Prod. Res.* **2019**, *33*, 3134–3142.
[36] D. Hülsewede, L. E. Meyer, J. von Langermann, *Chem. Eur. J.* **2019**, *25*, 4871–4884.
[37] S. Kille, C. G. Acevedo-Rocha, L. P. Parra, Z. G. Zhang, D. J. Opperman, M. T. Reetz, J. P. Acevedo, *ACS Synth. Biol.* **2013**, *2*, 83–92.
[38] E. Chovancova, A. Pavelka, P. Benes, O. Strnad, J. Brezovsky, B. Kozlikova, A. Gora, V. Sustr, M. Klvana, P. Medek, L. Biedermannova, J. Sochor, J. Damborsky, *PLoS Comput. Biol.* **2012**, *8*, e1002708.
[39] G. Li, P. Yao, R. Gong, J. Li, P. Liu, R. Lonsdale, Q. Wu, J. Lin, D. Zhu, M. T. Reetz, *Chem. Sci.* **2017**, *8*, 4093–4099.
[40] T. Hoshino, K. Shimizu, T. Sato, *Angew. Chem. Int. Ed.* **2004**, *43*, 6700–6703.
[41] M. Xu, P. R. Wilderman, R. J. Peters, *Proc. Natl. Acad. Sci. USA* **2007**, *104*, 7387–7401.

[42] K. C. Potter, J. Zi, Y. J. Hong, S. Schulte, B. Malchow, D. J. Tantillo, R. J. Peters, *Angew. Chem. Int. Ed.* **2016**, *55*, 634–638.
[43] S. C. Hammer, P.-O. Syrén, B. Hauer, *ChemistrySelect* **2016**, *1*, 3589–3593.
[44] P. M. Rodi, M. D. Bocco Gianello, M. C. Corregido, A. M. Gennaro, *Biochim. Biophys. Acta Biomembr.* **2014**, *1838*, 859–866.
[45] V. Kotov, K. Bartels, K. Veith, I. Josts, U. K. T. Subhramanyam, C. Günther, J. Labahn, T. C. Marlovits, I. Moraes, H. Tidow, C. Löw, M. M. Garcia-Alai, *Sci. Rep.* **2019**, *9*, 10379.
[46] M. Kadisch, M. K. Julsing, M. Schrewe, N. Jehmlich, B. Scheer, M. von Bergen, A. Schmid, B. Bühler, *Biotechnol. Bioeng.* **2017**, *114*, 874–884.
[47] C. W. Koo, F. J. Tucci, Y. He, A. C. Rosenzweig, *Science* **2022**, *375*, 1287–1291.
[48] J. Oliveira, E. Nogueira, G. A. Campolina, L. R. Batista, E. Alves, A. R. S. Caetano, R. M. Brandão, D. L. Nelson, M. D. G. Cardoso, *FEMS Microbiol. Lett.* **2021**, *368*, 1–9.
[49] A. C. Guimarães, L. M. Meireles, M. F. Lemos, M. C. C. Guimarães, D. C. Endringer, M. Fronza, R. Scherer, *Molecules* **2019**, *24*, 2471.
[50] R. N. Farías, B. Bloj, R. D. Morero, F. Siñeriz, R. E. Trucco, *Biochim. Biophys. Acta Rev. Biomembr.* **1975**, *415*, 231–251.
[51] Y. Meng, X. Shao, Y. Wang, Y. Li, X. Zheng, G. Wei, S. W. Kim, C. Wang, *Biotechnol. Bioeng.* **2020**, *117*, 3499–3507.
[52] B. Hauer, *ACS Catal.* **2020**, *10*, 8418–8427.
[53] M. K. Julsing, M. Schrewe, S. Cornelissen, I. Hermann, A. Schmid, B. Bühler, *Appl. Environ. Microbiol.* **2012**, *78*, 5724–5733.
[54] A. I. Benítez-Mateos, A. Schneider, E. Hegarty, B. Hauer, F. Paradisi, *Nat. Commun.* **2022**, *13*, 6269.
[55] P. Weber, M. Wagner, H. Schneckenburger, *J. Biomed. Opt.* **2010**, *15*, 046017.
[56] P. D. Kiser, M. Golczak, D. T. Lodowski, M. R. Chance, K. Palczewski, *Proc. Natl. Acad. Sci. USA* **2009**, *106*, 17325–17330.
[57] M. Golczak, P. D. Kiser, D. T. Lodowski, A. Maeda, K. Palczewski, *J. Biol. Chem.* **2010**, *285*, 9667–9682.
[58] P. H. Nguyen, A. Ramamoorthy, B. R. Sahoo, J. Zheng, P. Faller, J. E. Straub, L. Dominguez, J. E. Shea, N. V. Dokholyan, A. de Simone, B. Ma, R. Nussinov, S. Najafi, S. T. Ngo, A. Loquet, M. Chiricotto, P. Ganguly, J. McCarty, M. S. Li, C. Hall, Y. Wang, Y. Miller, S. Melchionna, B. Habenstein, S. Timr, J. Chen, B. Hnath, B. Strodel, R. Kayed, S. Lesné, G. Wei, F. Sterpone, A. J. Doig, P. Derreumaux, *Chem. Rev.* **2021**, *121*, 2545–2647.
[59] M. Ashtari, E. S. Nikonova, K. A. Marshall, G. J. Young, P. Aravand, W. Pan, G. shuang Ying, A. E. Willett, M. Mahmoudian, A. M. Maguire, J. Bennett, *Ophthalmology* **2017**, *124*, 873–883.
[60] E. Winkler, F. Kamp, J. Scheuring, A. Ebke, A. Fukumori, H. Steiner, *J. Biol. Chem.* **2012**, *287*, 21326–21334.

Manuscript received: February 2, 2023
Accepted manuscript online: March 20, 2023
Version of record online: April 18, 2023